Geophysical Research Letters

Supporting Information for

Global analysis of surface ocean CO_2 fugacity and air-sea fluxes with low latency

T. T. T. Chau[1], F. Chevallier[1], and M. Gehlen[1]

[1]Laboratoire des Sciences du Climat et de l'Environnement, LSCE/IPSL, CEA-CNRS-UVSQ, Université Paris-Saclay, F-91191 Gif-sur-Yvette, France

Contents of this file

1. Evaluation and analysis for surface ocean CO_2 fugacity and air-sea fluxes
2. Tables S1 to S5
3. Figures S1 to S10
4. References

1. Evaluation and analysis for surface ocean CO_2 fugacity and air-sea fluxes

1.1. Quality assessment for regional reconstruction and prediction of CO_2 fugacity (fCO_2)

In reconstruction mode (1985-2020), FFNNv2021 and FFNNv2 models perform with good skill over many ocean provinces (Figures 2, S3, and S5). Subtropical and tropical provinces (i.e., 3.NA-PS, 5.SA, 7.NP-PS, 8.PEQU-W, 10.SP, and 12.SIO) have the highest model skill among the ocean basins (RMSD < 14 µatm and r^2 > 0.74). Interestingly, these sub-basins are not dominant in data density compared to subpolar regions (2.NA-SS and 6.NP-SS) for the northern hemisphere and to the southern ocean (13.SO-SS) for the southern hemisphere (Figure 2). Data-rich provinces involve many observations distributed in coastal bands or in ocean upwelling systems with substantial fCO_2 inter-annual variations. These data put high weight on the calculated model-data mismatch (Figures S5 and S6). The model tends to get high biases from SOCAT data outliers (Figure S3), i.e., data beyond the 95% confidence interval ([279, 443] µatm) of the full data range. Overestimates of fCO_2 with a model-data bias greater than 100 µatm are distributed along the Arctic (1.ARC) and the subpolar-polar regions (2.NA-SS, 6.NP-SS, and 14.SO-ICE) (Figure S3 and Figure S5). Most of the poor estimates of fCO_2 belong to the coastal sector of these regions (Figure S5) where fCO_2 is characterized with high variability driven by multiple and complex physical and biological conditions (Feely et al., 2008; Bakker et al., 2016; Chavez et al., 2018; Chau et al., 2022). RMSD ranges from 21.1 µatm to 40 µatm and r^2 is between 0.57 and 0.76 over these regimes. In contrast, the FFNN models underestimate SOCAT fCO_2 at the right tail of its global distribution. Most of these data belong to the coastal sectors of NA-SS and NP-SS or are found in PEQU-E and NIO (see further analysis in Chau et al. (2022). Among these provinces, the eastern equatorial Pacific (9.PEQU-E) yields the largest RMSD (~27 µatm). Nevertheless, the reconstruction of the interannual variability of fCO_2 over PEQU-E has an r^2 of 0.71.

Despite general good performance as analyzed in the main manuscript, FFNNv2021 shows the poorest one-year prediction in 2021 relative to the 1985-2020 reconstruction skill in ARC (RMSD: 49.1 µatm vs 40 µatm; r^2: 0.25 vs 0.57), in AEQU (RMSD: 34.2 µatm vs 19.96 µatm; r^2: 0.36 vs 0.57), and in PEQU-E (RMSD: 37.2 µatm vs 27 µatm; r^2: 0.55 vs 0.71). The FFNNv2022 model reconstruction in 2021 benefits from more than 919 additional data (411 data points in the year 2021), resulting in an improvement in the fCO2 estimates in 2021 over the Arctic: the RMSD reduces to 41.8 µatm and r^2 rises up to 0.35 (Figure S7). In 2022, the FFNNv2022 model scores slightly better in one-year prediction (RMSD = 37.0 µatm and r^2 = 0.60) relative to the FFNNv2021 two-year prediction (RMSD = 37.7 µatm and r^2 = 0.56). To a smaller extent, this improvement holds for the equatorial Atlantic (4.AEQU) and the eastern equatorial Pacific (9.PEQU-E). For instance, the FFNNv2021 prediction (RMSD = 34.2 µatm and r^2 = 0.36) in AEQU in 2021 shows similar skill scores compared to the FFNNv2022 reconstruction (RMSD = 32.9 µatm and r^2 = 0.43). By contrast, the two model predictions perform well in 2022 (RMSD < 17.5 µatm and r^2 < 0.6), knowing that the evaluation data in SOCATv2023 in the years 2021 and 2022 do not have the same quantity and distribution over AEQU as well as other ocean provinces (Table S4 and Figure S5). For both reconstruction and prediction modes, the two time series of the mean fCO_2 derived from the two models deviate in interannual variability of fCO_2 in the equatorial Atlantic (Figure S6). Over the equatorial Pacific (9.PEQU-E), FFNNv2022 predicts fCO_2 in 2022 with a high deviation from SOCAT data (RMSD = 47.1 µatm) but reproduces its temporal variations well (r^2 = 0.76). FFNNv2021 makes the two-year prediction (RMSD = 45.1 µatm and r^2 = 0.77) marginally more precise than the latest model. The contradictory effects observed in the two FFNN performances over the tropical regions (4.AEQU and 9.PEQU-E) may derive from the discrepancy in SOCAT data used for model fits from one to another version; e.g., SOCATv2022 removed 234 [164] data from the previous version over AEQU [PEQU-E] for the period 1985-2020 (7% [2%] of the total data in this region) and added 116 [180] data for the year 2021 (Figures S2 and S7 and Table S4).

1.2. Computation of air-sea fluxes (*fg*CO_2)

An air–sea flux density of CO_2 is calculated in $molC.m^{-2}.yr^{-1}$ by using the formulation as follows,

$$fgCO_2 = K \times dpCO_2 = k \times L \times (1 - f_{ice}) \times (pCO_2^{air} - pCO_2^{sea}), \quad (1)$$

where K is the gas transfer coefficient and $dpCO_2$ is the air-sea difference in partial pressure of CO_2 (pCO_2). K is the product of gas transfer velocity (k), temperature-dependent solubility of CO_2 (L), and sea ice coverage ratio (f_{ice}). L is estimated with sea surface temperature (Weiss, 1974) while the computation of k replies on a quadratic dependence of 10-m wind speed (Ho et al., 2006; Wanninkhof., 2014) and a scaling to match the global mean k of 16.5 $cm.h^{-1}$ (Naegler, 2009). The derivation of atmospheric partial pressure of CO_2 (pCO_2^{air}) comes from CO_2 mole fraction multiplied with total pressure in dry air conditions. pCO_2^{sea} is converted from FFNN fCO_2 following Körtzinger., (1999). Data products used in the air-sea flux calculation are presented in Table S1. Given flux density per grid cell ($fgCO_2^{(i)}$), an integration of CO_2 fluxes ($PgC.yr^{-1}$) over a region or the global ocean derives from

$$fgCO_2 = \sum_{i=1:N} fgCO_2^{(i)} \times A^{(i)}, \quad (2)$$

where $A^{(i)}$ is the area in m^2 of grid cell (i).

1.3. Multi-year time series of fCO_2 and $fgCO_2$

Figures S6 and S8 (right sector of the red vertical line) respectively show the time series of mean fCO_2 predicted with FFNNv2022 models and of $fgCO_2$ integrated over different provinces. fCO_2 predicted for 2022 continues to increase resulting in an increment of the global average of sea surface partial pressure of CO_2 (pCO_2^{sea}) of 2.9 µatm relative to the year 2021 (Table S5) and much higher than its global growth rate of 1.7 $µatm.yr^{-1}$ (2.0 $µatm.yr^{-1}$) estimated over the period 1985-2022 (2010s). The one-year increment in atmospheric pCO_2 (pCO_2^{air}) between the two years (2.5 µatm) is less than in pCO_2^{sea} implying a reduction in the global ocean uptake of CO_2 predicted for 2022 (2.25±0.5 $PgC.yr^{-1}$) compared to the previous year (2.36±0.43 $PgC.yr^{-1}$). When adjusting the estimated global net fluxes with the riverine outgassing of CO_2 of 0.65 $PgC.yr^{-1}$ (Regnier et al., 2022) and the total ocean surface area (FFNNv2022 data covers 95% of the global ocean), one obtains the estimates of anthropogenic ocean carbon uptake about 3.13±0.46 $PgC.yr^{-1}$ and 3.02±0.52 $PgC.yr^{-1}$ in 2021 and 2022, respectively. The non-increasing imprint in the ocean sink of anthropogenic CO_2 found in this study is consistent with the 2022 projection proposed by Friedlingstein et al, (2022): the anthropogenic ocean sink in 2021 was 2.9±0.4 $PgC.yr^{-1}$ remains unchanged for the year 2022. This evidence supports the hypothesis that the persistence of cooling climate patterns (La Niña conditions) weakened CO_2 ocean uptake in 2021-2022 (high peaks appeared in mid-2022, Figure S9). For January to August in 2023, FFNNv2022 predicts a global net flux of 2.45±0.56 $PgC.yr^{-1}$ (w.r.s.t., 3.23±0.59 $PgC.yr^{-1}$ for anthropogenic uptake) higher than the 8-month net flux in 2022 of 2.17±0.50 $PgC.yr^{-1}$ (w.r.s.t., 2.94±0.53 $PgC.yr^{-1}$ for anthropogenic uptake).

1.4. Substantial intra- to inter-annual changes of fCO_2 and air-sea fluxes ($fgCO_2$) at the eastern equatorial Pacific (EEP) driven by the El Niño Southern Oscillation (ENSO)

The ENSO phenomenon does not only constrain ocean CO_2 outgassing at the tropical Pacific air-sea interface but also strongly affects the global net CO_2 uptake (Rödenbeck et al., 2015; Chau et al., 2022; Friedlingstein et al., 2022). In El Niño conditions, warmer surface temperature weakens vertical upwelling of subsurface water rich in dissolved inorganic carbon (DIC) and nutrients, therefore, El Niño leads to lower surface partial pressure of CO_2 (Feely et al., 2006; Wang et al., 2015). A decrease of fCO_2 reached 410 µatm and the intra-annual variation of fCO_2 was as large as 40 µatm in the year 2015 (Figure S6) as the strongest El Niño events of the last decade happened (Figure S9a). The dampening fCO_2 resulted in a reduction of the EEP source of CO_2 and thus an enhancement in the global ocean CO_2 uptake (Figure S8). The net flux excessed -0.15±0.03 $PgC.yr^{-1}$ in 2015/2016 while the EEP normally released an average source of CO_2 of -0.31±0.02 $PgC.yr^{-1}$ in the last decade. The spatial pattern in Figure S9bc confirms that the El Niño events spreading until the 2016 summer probably reduced fCO_2 below 400 µatm ($fgCO_2$ < -0.5 $molC.m^{-2}.yr^{-1}$) around 90°W and 150°W westward. Later in this period, the opposite conditions - La Niña - triggered in the 2017 summer became dominant and fCO_2 was, for the first time, rising over 460 µatm in the 2018 spring. La Niña has turned back and governed since the year 2020 (Figure S9a). The cooling phase persisted in 2021 and reached its maximum in the 2022 spring-summer. Anomalies in fCO_2 enhancement have been found throughout the year 2021 (Figure S9(b,c)). Likewise, FNNNv2022 correspondingly projects extremely high fCO_2 exceeding 484 µatm ($fgCO_2$ < -2.5 $molC.m^{-2}.yr^{-1}$) in the eastern Niño3 and Niño4 sectors in the first half of 2022. By then, a reduction of fCO_2 is predicted according to the lessening cooling conditions.

2. Tables

Table S1. Input datasets used for reconstructions and prediction of surface ocean CO_2 fugacity (fCO_2) and air-sea fluxes ($fgCO_2$) in 1985-2023.

Variables	Notation	Product name	References
Measurements of CO_2 fugacity	fCO_2	Surface ocean CO2 ATlas (SOCAT): SOCATv2021, SOCATv2022 (last access 17/06/2022), and SOCATv2023 (last access 20/06/2023)	Bakker et al. (2021, 2022, 2023)
Sea surface temperature	SST	Copernicus Marine Service (CMEMS): SST_GLO_SST_L4_REP_OBSERVATIONS_010_011 (1985-2021) SST_GLO_SST_L4_NRT_OBSERVATIONS_010_001 (2022-2023)	Good et al. (2020)
Sea ice fraction	f_{ice}		
Sea surface salinity	SSS	CMEMS: MULTIOBS_GLO_PHY_S_SURFACE_MYNRT_015_013 (1993-2023)	Buongiorno et al. (2016); Droghei et al. (2018)
Sea surface height	SSH	CMEMS: SEALEVEL_GLO_PHY_L4_MY_008_047 (1993-2021) SEALEVEL_GLO_PHY_L4_NRT_OBSERVATIONS_008_046 (2022-2023)	Pujol et al. (2016, 2018)

Mixed layer depth	MLD	Estimating the Circulation and Climate of the Ocean project Phase II (ECCO2): cube92_latlon_quart_90S90N (1992-2022)	Menemenlis et al. (2008)
Chlorophyll-*a*	Chl-*a*	CMEMS: OCEANCOLOUR_GLO_BGC_L4_MY_009_104 (1998-2023)	Garnesson et al . (2019)
Atmospheric CO_2 mole fraction	xCO_2	CO_2 atmospheric inversion from the Copernicus Atmosphere Monitoring Service (CAMS): Surface: v20r2 (1985-2020) Satellite: FT21r2 (2021)	Chevallier et al. (2005, 2010); Chevallier. (2013)
pCO_2 climatology	pCO_2^{clim}	Lamont Doherty Earth Observatory (LDEO) climatology of sea surface partial pressure of CO_2	Takahashi et al. (2009)
Wind speed	U	ERA5 hourly data on single levels from 1959 to present (1985-2023)	Hersbach et al., (2020)
Total pressure	Ps		

Notes:

- Preprocessing for missing data in the reconstruction mode (before the 2000s):
    - SSS and CHL-*a* (MLD) are set to climatologies computed on the available data (in 1992-1997).
    - SSH is set to climatologies plus linear trends computed on the available data
- Preprocessing for missing data in the prediction mode (2022-2023):

    Input datasets for prediction are set to the same data resources as for reconstruction, these data are available within a few weeks behind real time. This condition is not met for the xCO_2 and MLD datasets that we use in 2023. For xCO_2, we extrapolated the original dataset (the atmospheric inversion of the Copernicus Atmosphere Monitoring Service for years 1985- 2022, Table S1), knowing the recent measurements of the atmospheric CO_2 mole fraction at the Mauna Loa Observatory, Hawaii (https://gml.noaa.gov/ccgg/trends/mlo.html, last access: 11/9/2023). For MLD, given the dominance of seasonality in its variability (Menemenlis et al. 2008, Zhang et al. 2018), we use the last 5-year climatology of the Estimating the Circulation and Climate of the Ocean project Phase II (ECCO2) data in the prediction mode.

Table S2. Indicators of ocean provinces (Figure S1) used in this study.

No	Ocean provinces	Remarks
0	Global ocean (GLO)	

1	Arctic (ARC)	Aggregated from Arctic, North Atlantic, and North Pacific ice biomes and the Barents Sea (biomes 1, 2, 3, and 4)
2	North Atlantic seasonally stratified (NA-SS)	Aggregated from North Atlantic subpolar and subtropical seasonally stratified biomes (biomes 5 and 6)
3	North Atlantic permanently stratified (NA-PS)	North Atlantic subtropical permanently stratified biome (biome 7)
4	Atlantic equatorial (AEQU)	Biome 8
5	South Atlantic (SA)	South Atlantic subtropical permanently stratified biome (biome 9)
6	North Pacific seasonally stratified (NP-SS)	Aggregated from North Pacific subpolar and subtropical seasonally stratified biomes (biomes 11 and 12)
7	North Pacific permanently stratified (NP-PS)	North Pacific subtropical permanently stratified biome (biome 13)
8	Pacific western equatorial (PEQU-W)	Biome 14
9	Pacific eastern equatorial (PEQU-E)	Biome 15
10	South Pacific (SP)	South Pacific subtropical permanently stratified biome (Biome 16)
11	Northern Indian Ocean (NIO)	Aggregated from the Arabian Sea, Bay of Bengal, and Equatorial Indian Ocean above the Equator (biomes 17, 18, and 19)
12	Southern Indian Ocean (SIO)	Aggregated from the Equatorial Indian Ocean blow the Equator and the South Indian Ocean (biomes 19 and 20)
13	Southern Ocean seasonally stratified (SO-SS)	Aggregated from Southern Ocean subpolar and subtropical seasonally stratified biomes (biomes 21 and 22)
14	Southern Ocean icea (SO-ICE)	Biome 23

Table S3. Comparison of CMEMS-LSCE-FFNN models (FFNNv2021 and FFNNv2022)

a) Summary of SOCAT data used for model runs and model evaluation

FFNN	Model fitting			Model evaluation				
	Target Data	Time span	Number of data	Target Data	Reconstruction		Prediction	
					Time span	Number of data	Time span	Number of data

v2021	SOCATv2021	1985-2020	306357	SOCATv2023	1985-2020	302255	2021-2022	10908 8602
v2022	SOCATv2022	1985-2021	311694		1985-2021	313163	2022	8602

b) Model evaluation between global reconstructions of fCO_2 [μatm] in 1985-2020 and between FFNNv2021 prediction and FFNNv2022 reconstruction (prediction) in 2021 (2022). Statistics include the number of SOCAT monthly gridded data (N), mean fCO_2 (μ), mean uncertainty (σ), and model-data misfit (RMSD) and coefficient of determination (r^2).

FFNN	Years											
	1985-2020				2021				2022			
	μ	σ	RMSD	r^2	μ	σ	RMSD	r^2	μ	σ	RMSD	r^2
v2021	361.6	8.7	19.1	0.78	395.2	11.4	24.3	0.74	397.8	12.2	23.1	0.75
v2022	361.5	8.5	19.1	0.78	395.7	10.9	23.3	0.76	398.5	11.3	22.6	0.76

Table S4. **Regional comparison (a) between FFNN model reconstructions of fCO_2 [μatm] in 1985-2020, (b) between FFNNv2021 prediction and FFNNv2022 reconstruction in 2021, and (c) between FFNN model predictions in 2022. Statistics include 1) the number (N) of monthly gridded data used in FFNN fits (SOCATv2021 and SOCATv2022) and in data evaluation (SOCATv2023, see values in brackets), 2) mean fCO_2 (μ), 3) mean uncertainty (σ), and 4) model-data misfit (RMSD), and 5) determination coefficient (r^2).**

No	Biome	FFNN	Years														
			1985-2020					2021					2022				
			N	μ	σ	RMSD	r^2	N	μ	σ	RMSD	r^2	N	μ	σ	RMSD	r^2
1	ARC	v2021	5043 (5646)	320.5	30.0	40.0	0.57	0 (411)	356.3	31.3	49.1	0.25	0 (225)	351.4	29.6	37.7	0.56
		v2022	5551 (5646)	318.0	29.3	40.0	0.57	411 (411)	348.5	29.5	41.8	0.35	0 (225)	345.6	27.5	37.0	0.60
2	NA-SS	v2021	57808 (55738)	339.8	8.0	23.1	0.76	0 (2350)	368.8	9.0	26.0	0.76	0 (2265)	373.6	10.1	24.6	0.74

		v2022	55714 (55738)	339.9	7.7	23.1	0.76	2167 (2350)	369.1	8.3	26.2	0.75	0 (2265)	374. 8	9.1	24.0	0.75
3	NA-PS	v2021	37951 (37011)	364.5	5.3	13.9	0.74	0 (1161)	398.4	6.3	20.4	0.50	0 (1007)	401. 0	7.0	18.2	0.61
		v2022	36991 (37011)	364.5	5.1	13.8	0.75	945 (1161)	399.3	5.9	20.1	0.51	0 (1007)	402. 7	6.5	17.0	0.65
4	AEQU	v2021	3313 (3179)	376.9	10.0	20.0	0.57	0 (182)	400.2	12.8	34.2	0.36	0 (144)	403. 1	14.2	17.3	0.64
		v2022	3179 (3179)	376.0	10.0	19.9	0.57	116 (182)	400.5	13.2	32.9	0.43	0 (144)	404. 2	13.6	16.7	0.65
5	SA	v2021	6575 (6497)	369.6	7.9	13.2	0.79	0 (273)	398.5	9.5	14.3	0.55	0 (161)	401. 1	10.2	12.8	0.51
		v2022	6497 (6497)	369.7	7.6	12.9	0.80	212 (273)	401.9	9.2	12.4	0.59	0 (161)	404. 3	9.6	12.0	0.55
6	NP-SS	v2021	57531 (58165)	349.1	8.2	21.1	0.73	0 (2334)	378.9	10.1	28.3	0.76	0 (1495)	383. 1	11.1	31.0	0.62
		v2022	58161 (58165)	349.5	8.0	21.0	0.74	2147 (2334)	380.8	9.4	27.4	0.77	0 (1495)	385. 9	10.2	30.2	0.64
7	NP-PS	v2021	40176 (40300)	360.7	5.3	11.9	0.85	0 (1705)	397.0	7.1	16.4	0.76	0 (1608)	401. 3	8.4	13.2	0.78
		v2022	40287 (40300)	360.6	5.1	11.8	0.85	1443 (1705)	397.1	6.5	16.1	0.77	0 (1608)	401. 5	7.3	12.4	0.81
8	PEQU-W	v2021	14845 (14821)	366.6	6.1	11.2	0.72	0 (484)	407.2	9.2	11.2	0.76	0 (326)	411. 6	10.7	12.0	0.73
		v2022	14821 (14821)	366.6	6.0	11.2	0.72	430 (484)	407.8	8.2	11.1	0.74	0 (326)	411. 8	9.1	10.9	0.78
9	PEQU-E	v2021	9470 (9306)	415.7	9.9	27.0	0.71	0 (199)	460.0	14.4	37.2	0.55	0 (146)	462. 4	15.7	45.0	0.77
		v2022	9306 (9306)	415.5	9.7	26.9	0.71	180 (199)	459.8 9	13.1	35.2	0.59	0 (146)	461. 9	13.8	47.1	0.76
10	SP	v2021	21551 (20968)	363.1	9.0	11.9	0.86	0 (689)	398.4	11.9	10.2	0.85	0 (592)	399. 8	12.6	10.1	0.80
		v2022	20968 (20968)	363.5	8.8	11.8	0.87	605 (689)	399.3	11.3	9.8	0.86	0 (592)	400. 5	11.5	10.0	0.80
11	NIO	v2021	1335 (1335)	382.8	15.0	24.0	0.53	0 (0)	418.3	23.6	nan	nan	0 (0)	419. 8	24.4	nan	nan
		v2022	1335 (1335)	382.1	14.7	23.9	0.54	0 (0)	416.8	23.7	nan	nan	0 (0)	419. 7	23.4	nan	nan
12	SIO	v2021	4583 (4562)	357.2	9.3	10.8	0.88	0 (133)	392.6	14.1	11.2	0.80	0 (73)	394. 1	14.8	8.8	0.43
		v2022	4562 (4562)	356.7	9.0	10.8	0.88	133 (133)	392.8	13.8	12.0	0.81	0 (73)	394. 2	13.6	9.3	0.45

Table S5. Area-integrated air-sea CO_2 fluxes ($fgCO_2$) derived from FFNNv2022 fCO_2 reconstruction in 1985-2021 and from FFNNv2022 predictions in 2022-2023. The units of $fgCO_2$ are in $PgC.yr^{-1}$. Area-averaged surface temperature (SST), 10-m wind speed (U), sea surface partial pressure of CO_2 (pCO_2^{sea}), air-sea pCO_2 difference ($dpCO_2$), and gas transfer coefficient (K) are provided for the global ocean and each ocean province (see province indicator in Figure S1).

No	Biome	Area [10^6 km^2]	Years	Variables					
				SST [°C]	U [ms^{-1}]	pCO_2^{sea} [µatm]	$dpCO_2$ [µatm]	K [$molC.m^{-2}.yr^{-1}.\mu atm^{-1}$]	$fgCO_2$ [$PgC.yr^{-1}$]
0	**GLO**	343.3	1985-2020	18.8	7.8	362.8±10.5	2.8	0.0526	1.583±0.341
			2021	19.0	7.9	397.1±13.0	6.0	0.0524	2.355±0.434
			2022	19.2	7.9	400.0±13.0	5.7	0.0528	2.249±0.495
			2023/01-08	19.1	7.8	401.5±14.1	7.0	0.0519	2.449±0.557
1	**ARC**	6.9	1985-2020	-0.5	7.3	324.9±33.3	50.3	0.0228	0.082±0.017
			2021	-0.1	7.5	355.5±34.2	55.9	0.026	0.107±0.020
			2022	-0.1	7.5	356.4±32.6	60.0	0.0281	0.106±0.017
			2023/01-08	-0.5	6.5	366.0±39.9	53.8	0.0137	0.077±0.015
2	**NA-SS**	15.9	1985-2020	11.8	9.2	341.2±9.5	30.4	0.0733	0.384±0.041
			2021	12.3	9.4	370.4±9.8	38.6	0.0750	0.503±0.045
			2022	12.5	9.3	376.1±10.4	37.0	0.0731	0.475±0.048
			2023/01-08	12.0	9.0	376.2±11.2	39.4	0.0697	0.467±0.052

3	**NA-PS**	22.2	1985-2020	25.1	7.0	365.7±5.9	0.8	0.0397	0.042±0.025
			2021	25.4	7.0	400.6±6.6	3.1	0.0389	0.064±0.027
			2022	25.4	6.9	403.6±7.0	3.5	0.0383	0.073±0.031
			2023/01-08	25.4	6.8	404.2±7.7	5.8	0.037	0.092±0.034
4	**AEQU**	8.5	1985-2020	26.9	5.5	377.2±12.5	-14.2	0.0254	-0.040±0.010
			2021	27.4	5.5	401.8±15.5	-1.9	0.0251	-0.009±0.017
			2022	27.2	5.5	405.9±15.5	-3.5	0.0245	-0.012±0.016
			2023/01-08	27.6	5.4	404.0±17.1	0.6	0.0241	-0.002±0.018
5	**SA**	19.5	1985-2020	22.6	7.2	371.0±8.5	-5.2	0.0419	-0.012±0.033
			2021	22.8	7.3	403.2±10.1	0.5	0.0423	0.049±0.048
			2022	22.8	7.2	405.6±10.6	-0.4	0.0406	0.036±0.047
			2023/01-08	23.5	7.1	411.0±11.8	-2.9	0.0405	0.024±0.059
6	**NP-SS**	24.7	1985-2020	12.7	8.7	350.8±10.2	21.4	0.0651	0.393±0.056
			2021	13.3	8.5	382.2±11.8	27.6	0.0618	0.476±0.060
			2022	13.6	8.6	387.6±12.0	26.4	0.0632	0.477±0.073
			2023/01-08	12.6	8.3	389.1±13.0	27.8	0.0589	0.436±0.078
7	**NP-PS**	40.2	1985-2020	26.3	7.0	361.7±6.1	2.9	0.0404	0.130±0.040
			2021	26.4	6.9	398.4±7.6	3.7	0.0388	0.152±0.053
			2022	26.5	6.8	402.8±8.2	2.5	0.0373	0.126±0.052
			2023/01-08	26.1	7.1	403.4±8.6	5.1	0.0412	0.176±0.069
8	**PEQU-W**	13.1	1985-2020	29.3	5.1	367.7±7.6	-7.9	0.0220	-0.023±0.010
			2021	29.4	5.2	409.0±9.4	-12.4	0.0222	-0.040±0.013
			2022	29.3	5.4	413.3±10.0	-14.0	0.0236	-0.052±0.016
			2023/01-08	29.5	5.2	412.1±10.7	-10.2	0.0227	-0.036±0.016
9	**PEQU-E**	15.1	1985-2020	26.3	5.9	416.8±10.8	-54.0	0.0292	-0.294±0.023
			2021	25.9	6.3	461.3±14.2	-60.8	0.0314	-0.350±0.030
			2022	25.6	6.4	463.5±15.0	-60.4	0.0328	-0.370±0.037

			2023/01-08	27.5	5.8	460.2±15.0	-55.7	0.0277	-0.297±0.036
10	**SP**	54.8	1985-2020	22.0	7.5	364.7±9.9	0.1	0.0470	0.103±0.117
			2021	22.1	7.6	400.6±12.4	2.6	0.0468	0.161±0.146
			2022	22.0	7.6	401.9±12.5	3.3	0.0464	0.166±0.146
			2023/01-08	22.8	7.5	405.0±13.3	2.2	0.0463	0.201±0.168
11	**NIO**	11.4	1985-2020	28.2	6.0	383.3±17.0	-21.7	0.0317	-0.113±0.042
			2021	28.5	6.0	418.1±25.8	-19.8	0.0305	-0.099±0.077
			2022	28.4	6.0	421.1±25.2	-20.1	0.0311	-0.104±0.075
			2023/01-08	28.6	6.0	421.3±23.8	-17.4	0.0324	-0.096±0.076
12	**SIO**	32.9	1985-2020	24.8	7.1	357.8±9.6	5.8	0.0421	0.187±0.064
			2021	25.0	7.2	394.0±14.8	7.1	0.0422	0.216±0.114
			2022	24.9	7.2	395.4±14.5	7.6	0.0423	0.223±0.119
			2023/01-08	25.3	7.1	397.9±13.8	8.1	0.0414	0.222±0.109
13	**SO-SS**	59.6	1985-2020	8.0	10.5	353.0±9.4	13.3	0.0951	0.721±0.185
			2021	8.2	10.7	386.2±11.6	18.0	0.0956	1.006±0.232
			2022	8.2	10.7	388.4±12.1	17.8	0.0955	0.980±0.269
			2023/01-08	8.7	10.6	391.7±13.4	17.8	0.0950	1.006±0.314
14	**SO-ICE**	17.3	1985-2020	-1.1	9.1	366.1±11.9	-5.0	0.0421	0.022±0.040
			2021	-1.0	9.1	392.3±14.0	5.2	0.0423	0.119±0.042
			2022	-1.0	9.5	394.4±14.6	4.7	0.0525	0.122±0.054
			2023/01-08	-0.7	9.4	392.3±14.7	11.1	0.0575	0.175±0.073

3. Figures

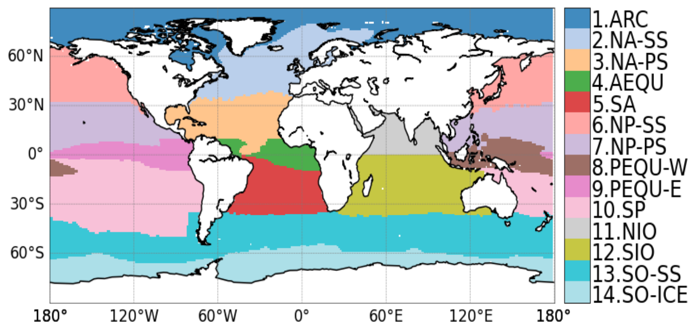

Figure S1. **Ocean provinces aggregated from the biomes used in the RECCAP2 project (source: https://github.com/RECCAP2-ocean/RECCAP2-shared-resources/tree/master/data/regions, last access: 20/3/2023). See Table S2 for the province indicator.**

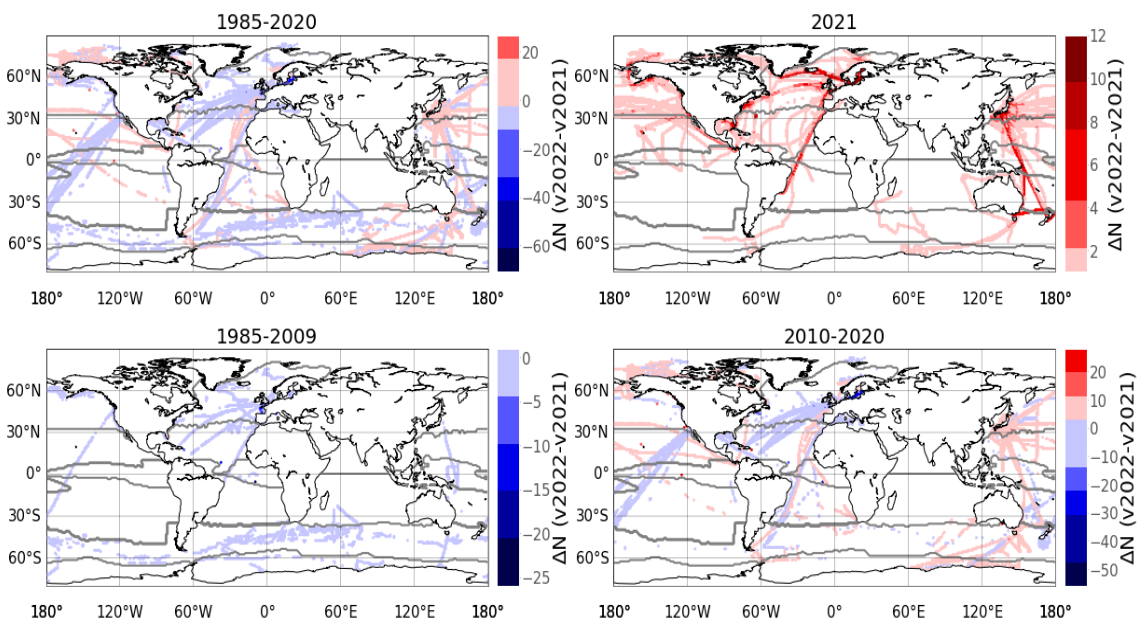

Figure S2. **Number of fCO_2 data (ΔN) added in (red) or removed from (blue) SOCATv2022 compared to SOCATv2021 for different time frames.**

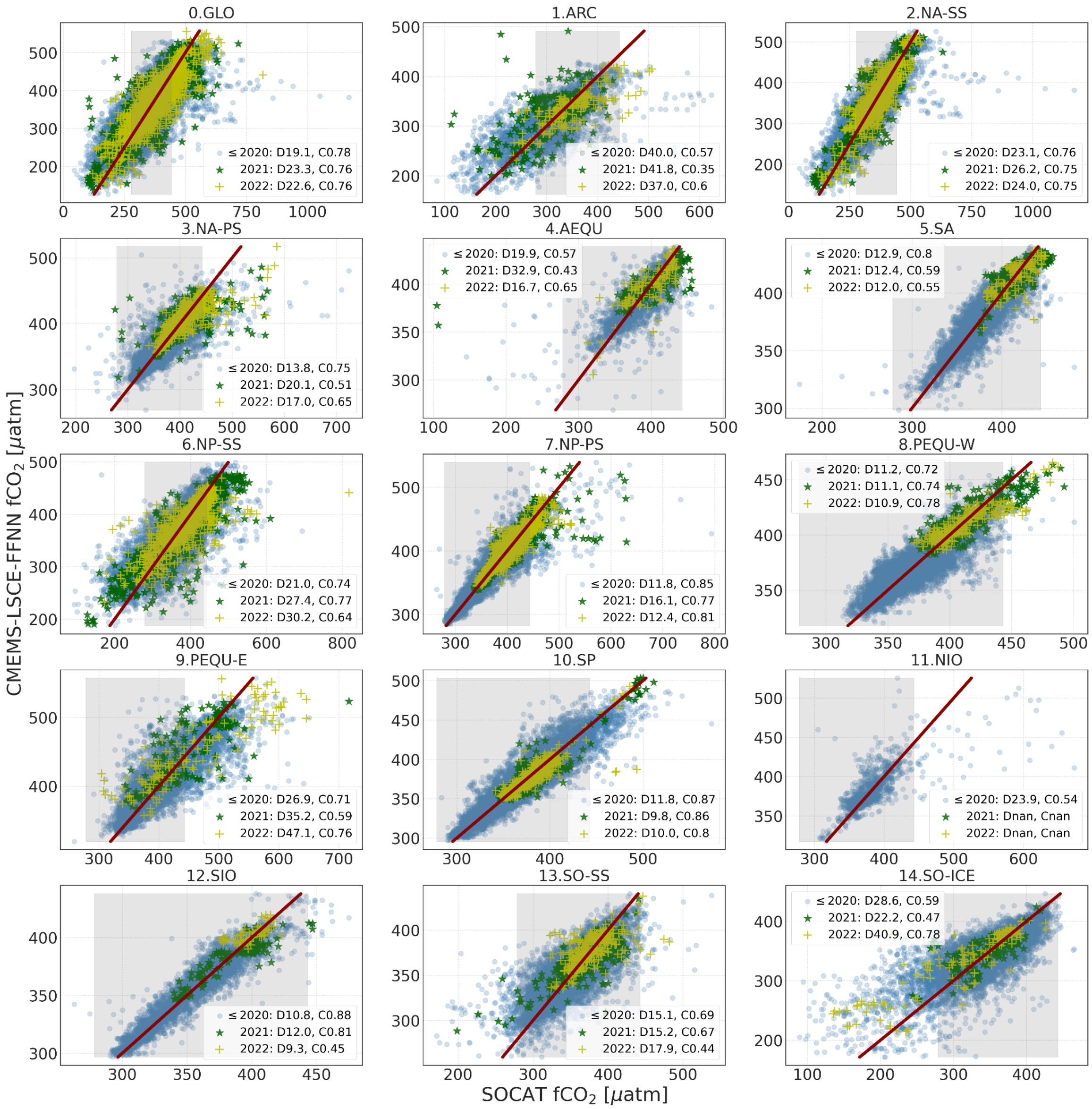

Figure S3. **Scatter plots of FFNNv2022 versus SOCATv2023 *f*CO_2 [µatm] for 36-year reconstruction (1985-2020: points), 1-year reconstruction (2021: stars) and 1-year prediction (2022: pluses). Values of FFNNv2022 and SOCATv2023 data are shown in y- and x-axis, respectively. Light-grey rectangles mark the 95% SOCAT data range (i.e., [279, 443] µatm) over the global ocean in 1985-2021. Red lines represent the bisector corresponding to ideal model-data fits: objects above this line indicate FFNN overestimates of SOCAT *f*CO_2 and vice versa. Metrics for reconstruction and prediction in the legend are model-data standard deviation (D: RMSD) and correlation (C: r^2).**

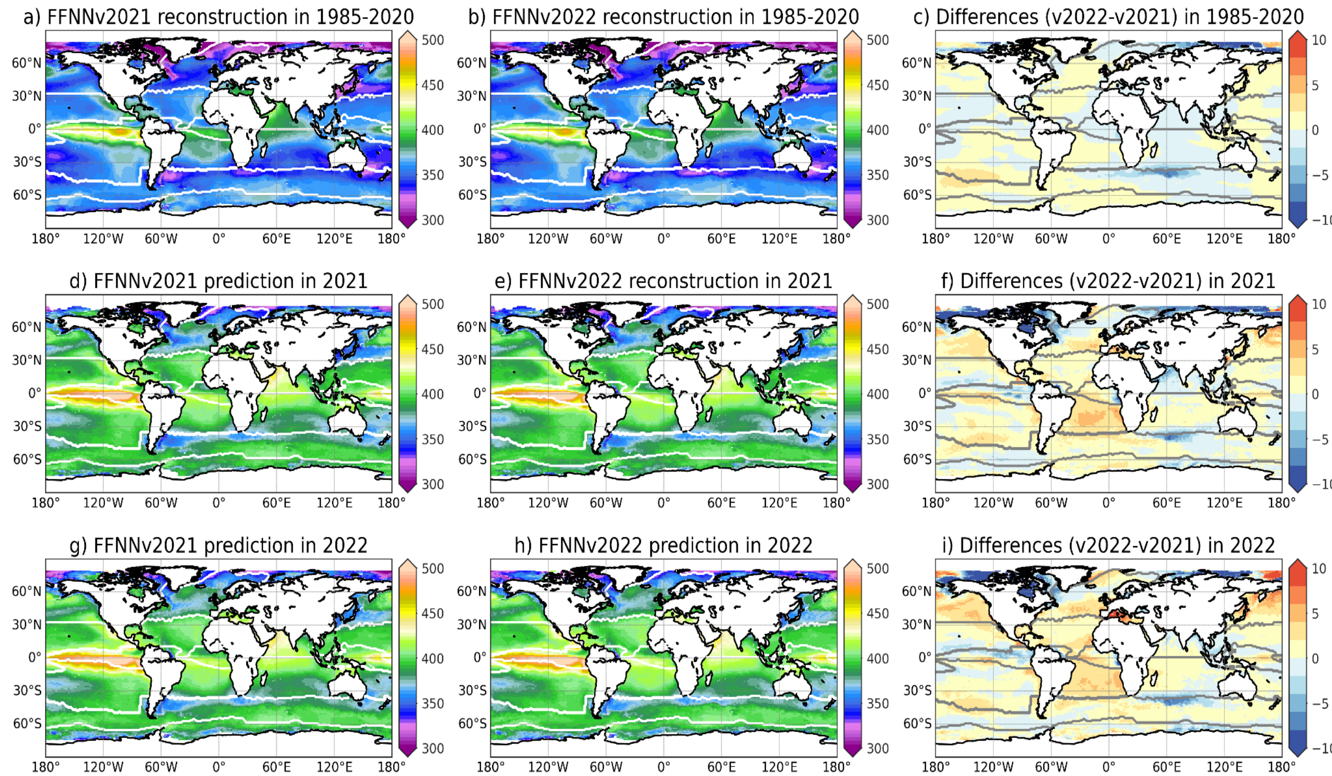

Figure S4. Spatial distribution of temporal means of *f*CO_2 [µatm] derived from FFNNv2021 (left) and FFNNv2022 (middle) and their discrepancy (right).

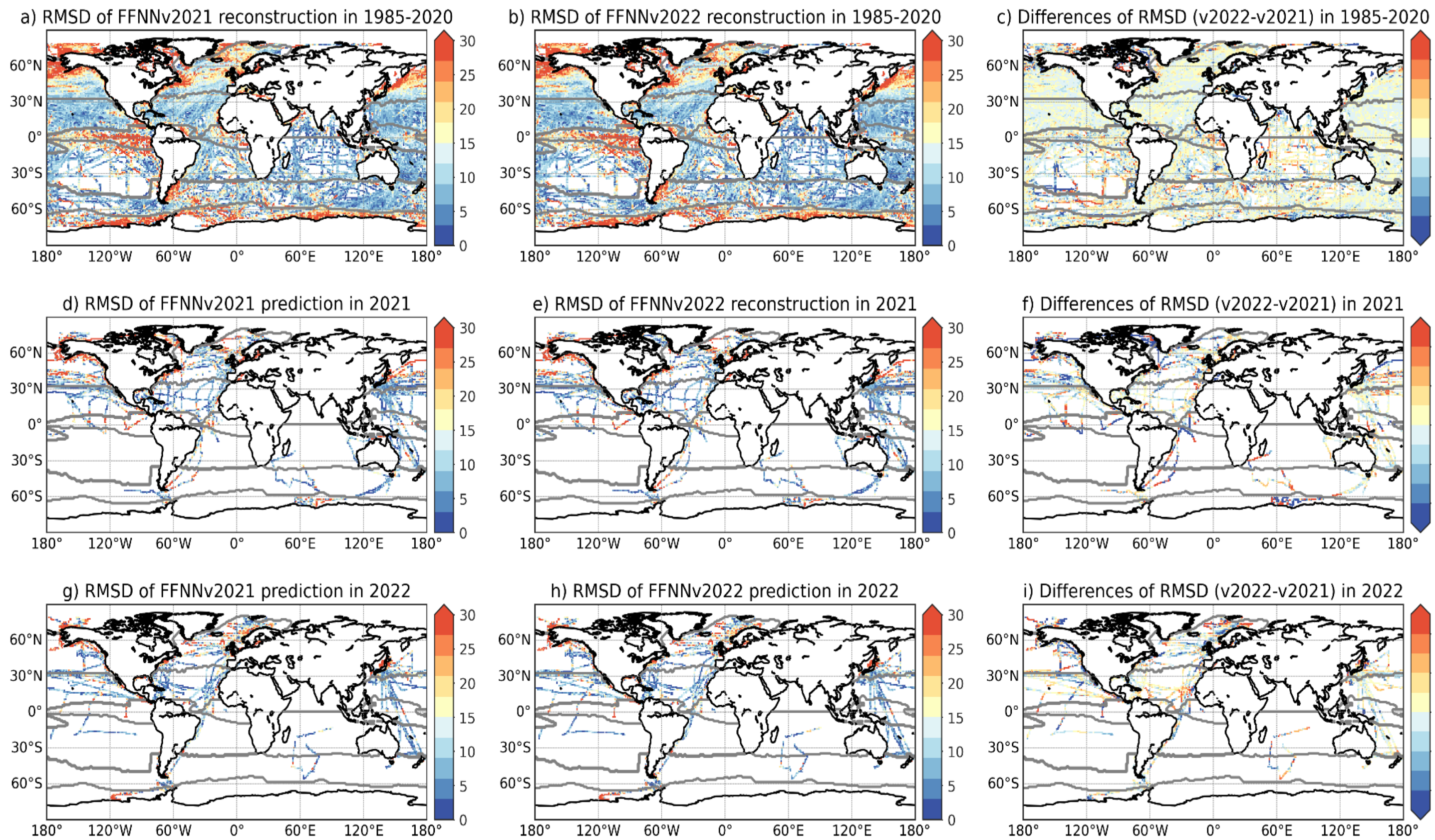

Figure S5. **Spatial distribution of model-data deviation (RMSD) in μatm: fCO_2 derived from FFNNv2021 (left) and FFNNv2022 (middle) and their RMSD difference (right). SOCATv2023 is used for this evaluation.**

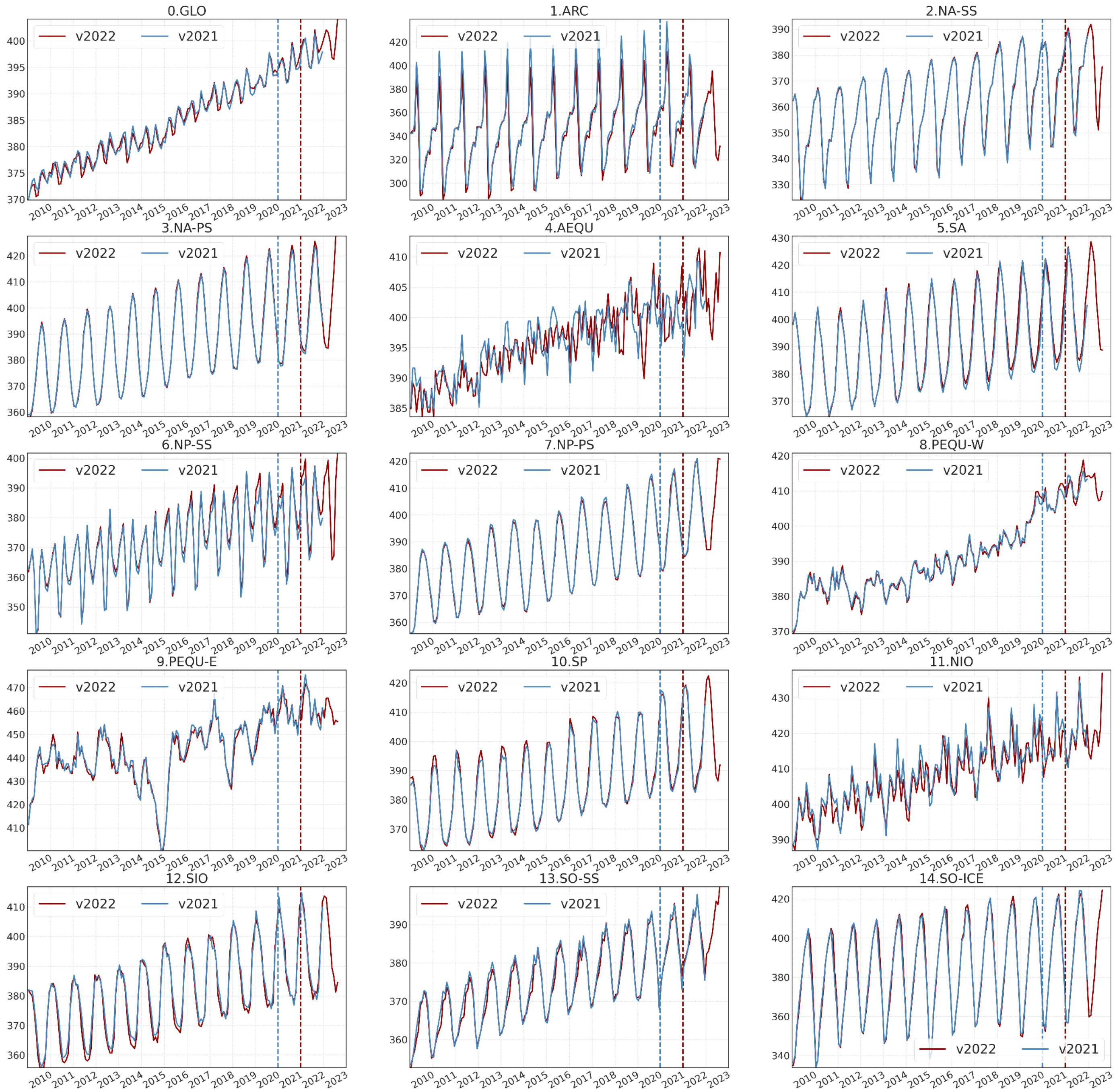

Figure S6. Time series of fCO_2 [μatm] averaged over ocean provinces. Vertical dashed lines mark the starting date for model prediction (blue: FFNNv2021, red: FFNNv2022).

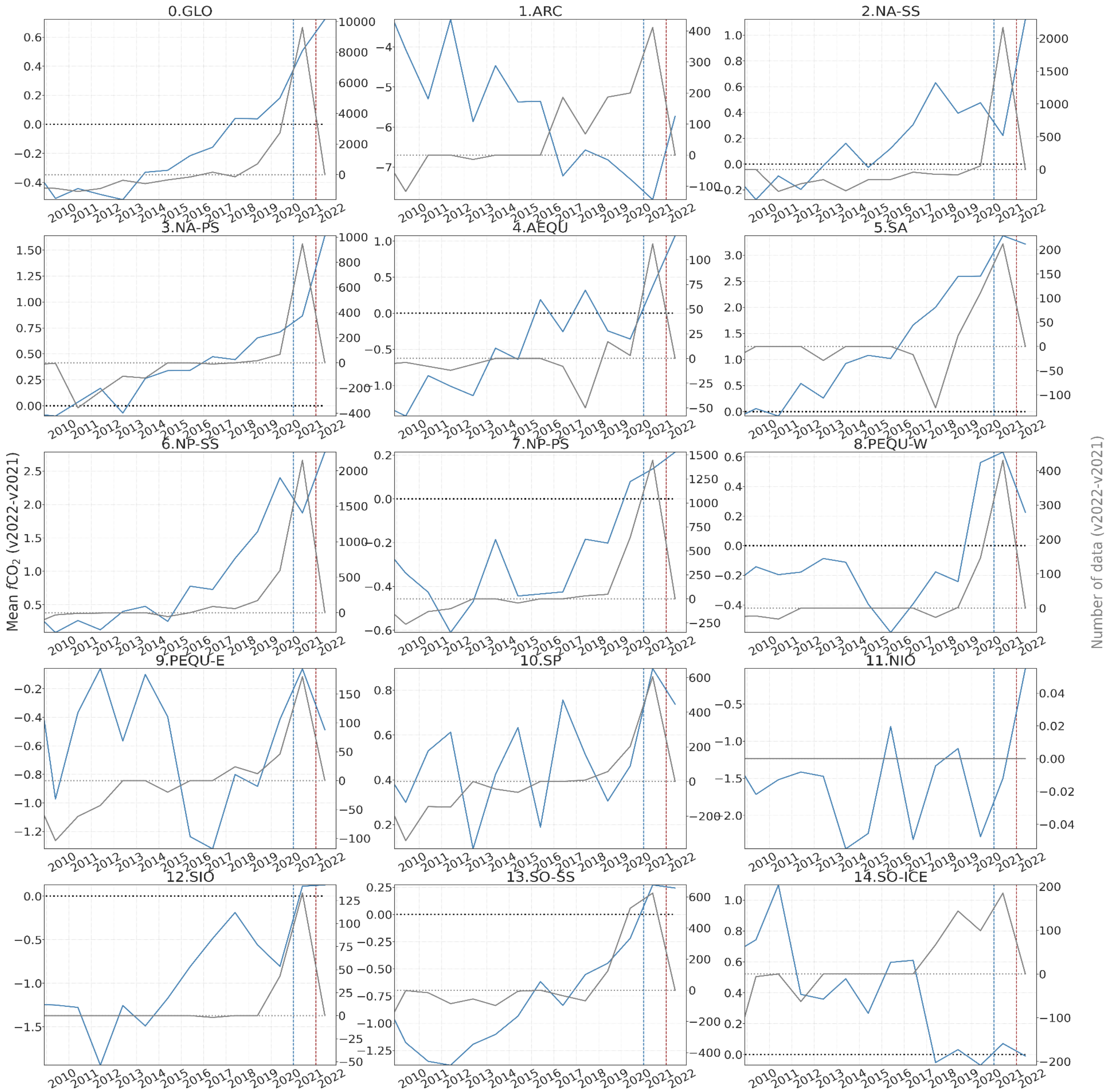

Figure S7. Time series of differences in *f*CO_2 [µatm] (left y-axis) and number of SOCAT data (right y-axis). Vertical dashed line marks the starting date for prediction (FFNNv2021: blue, FFNNv2022: red).

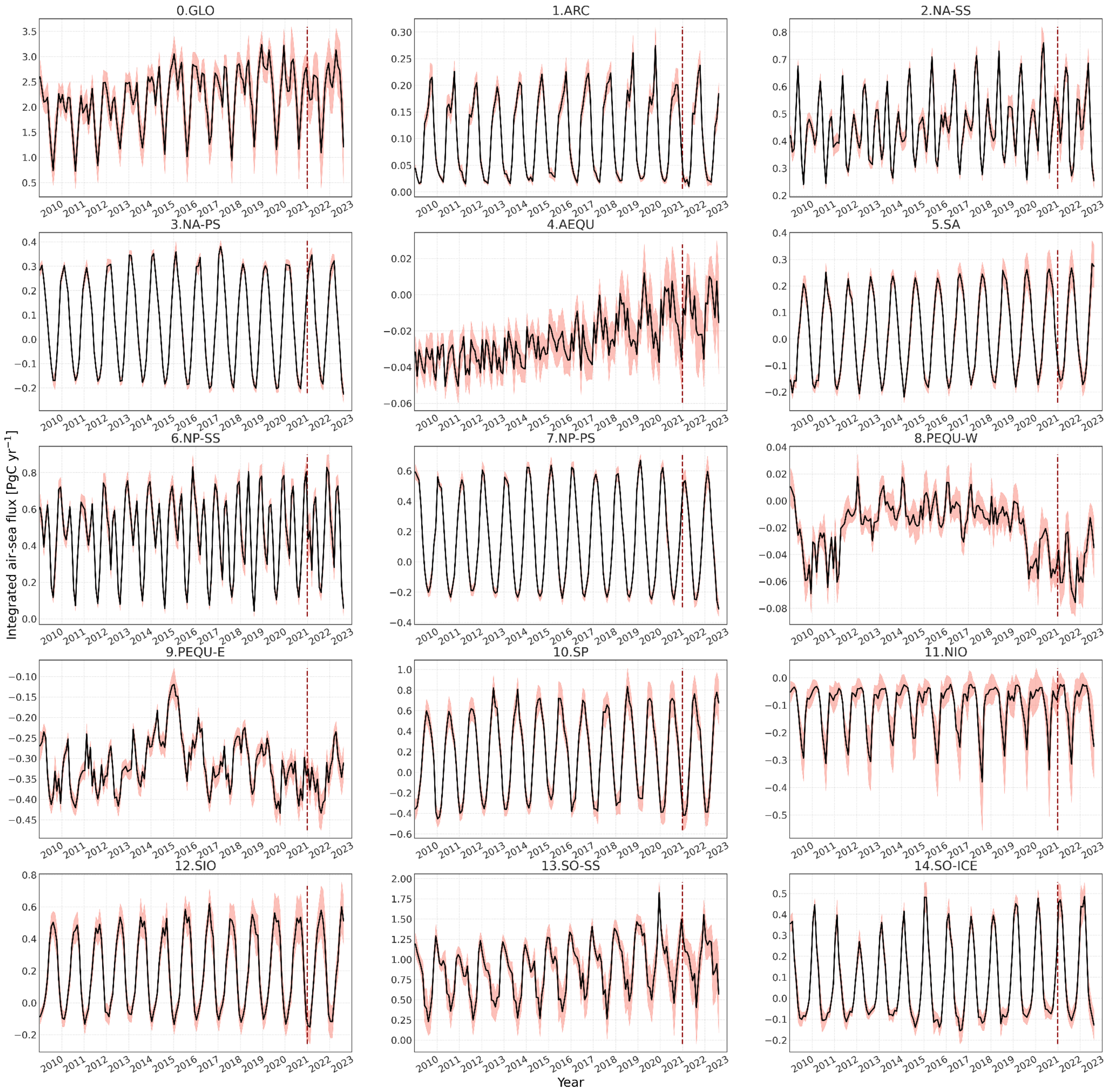

Figure S8. Time series of monthly air-sea fluxes integrated over ocean provinces [PgC.yr^{-1}]. Plain curve and shaded area represent model's best estimate and 1σ-uncertainty. Vertical dashed lines mark the starting date for FFNNv2022 prediction.

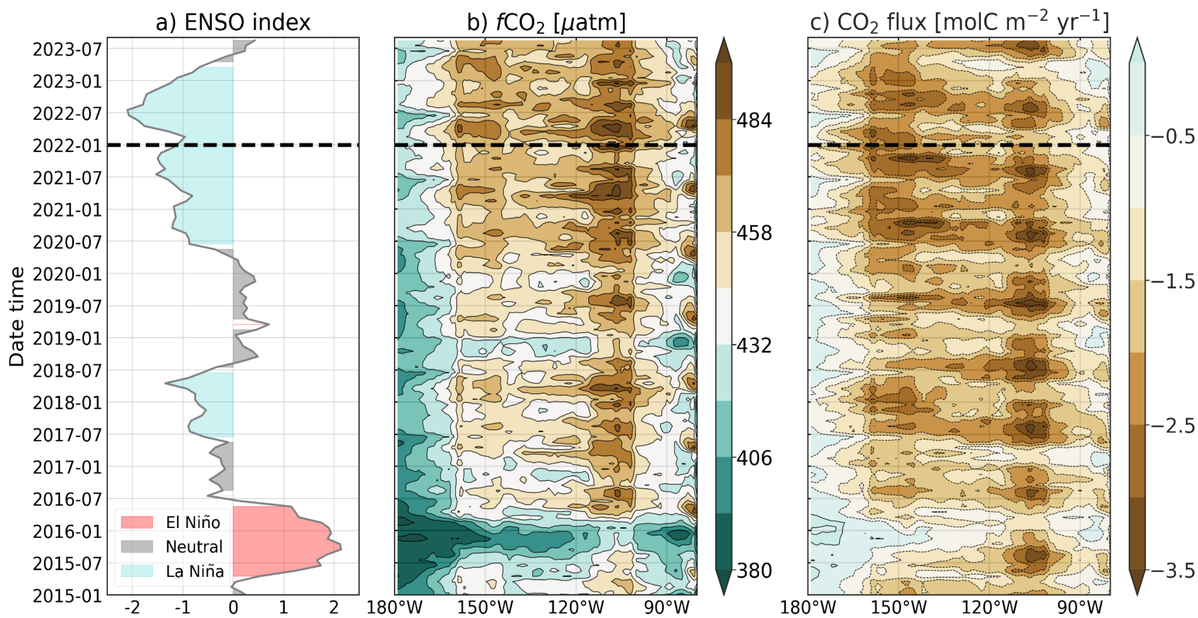

Figure S9. **Illustration of the relationship between ENSO events (a) and FFNNv2022 fCO_2 (air-sea fluxes) variations (Hovmöller plots in b and c) over the eastern Equatorial Pacific (9.PEQU-E). ENSO events are plotted with the NOAA bi-monthly Multivariate El Niño/Southern Oscillation (ENSO) index (https://psl.noa35.5, 50.5a.gov/enso/mei/, last access: 11/09/2023). The black horizontal dotted line marks the starting date for the FFNNv2022 prediction (January 2022).**

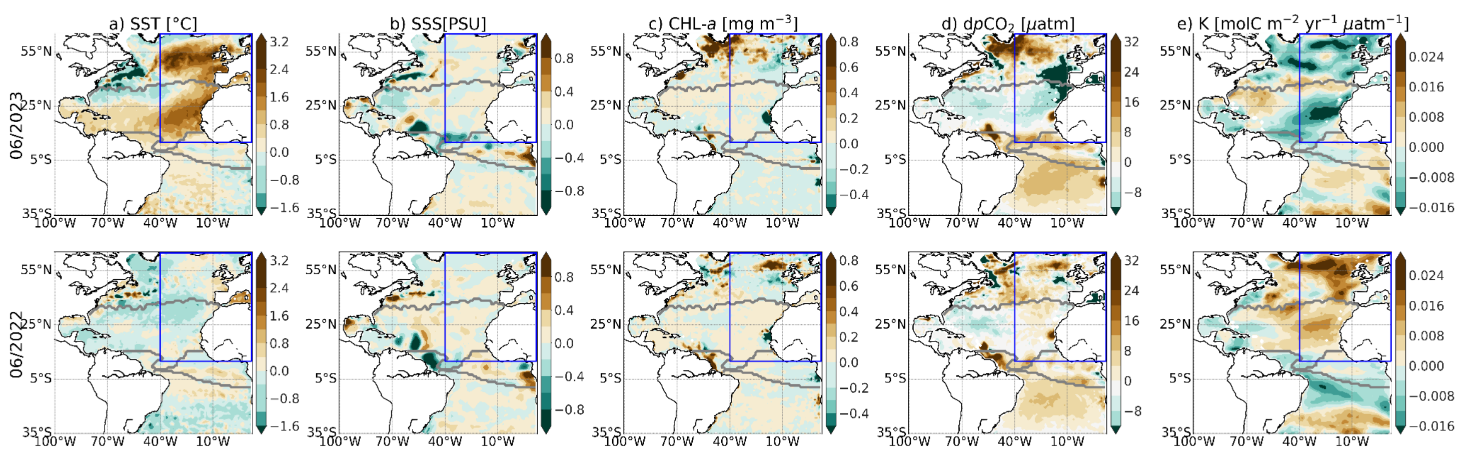

Figure S10. **Anomalies of surface temperature (SST), salinity (SSS), Chlorophyll-*a* (CHL-*a*), air-sea pCO_2 difference (dpCO_2), gas transfer coefficient (K) over the Atlantic in June 2023 (top) and June 2022 (bottom) are computed by subtracting long-term trends and seasonal climatologies relative to the years 1985-2022. Blue box limits the region of interest where the extreme marine heat wave appeared in the northeastern Atlantic in June 2023.**

References

Bakker, D., Alin, S., Becker, M., Bittig, H., Castaño-Primo, R., Feely, R. A., Gritzalis, T., Kadono, K., Kozyr, A., Lauvset, S. K., Metzl, N., Munro, D., Nakaoka, S.-i., Nojiri, Y., O'Brien, K., Olsen, A., Pfeil, B., Pierrot, D., Steinhoff, T., Sullivan, K., Sutton, A., Sweeney, C., Tilbrook, B., Wada13, C., Wanninkhof, R., Wranne, A. W., et al. (2023). SOCAT version 2021 for quantification of ocean CO2 uptake [Dataset]. https://www.socat.info/wp-content/uploads/2022/06/2022_Poster_SOCATv2021_release.pdf

Bakker, D., Alin, S., Becker, M., Bittig, H., Castaño-Primo, R., Feely, R. A., Gritzalis, T., Kadono, K., Kozyr, A., Lauvset, S. K., Metzl, N., Munro, D., Nakaoka, S.-i., Nojiri, Y., O'Brien, K., Olsen, A., Pfeil, B., Pierrot, D., Steinhoff, T., Sullivan, K., Sutton, A., Sweeney, C., Tilbrook, B., Wada13, C., Wanninkhof, R., Wranne, A. W., et al. (2022). SOCAT version 2022 for quantification of ocean CO2 uptake [Dataset]. https://www.socat.info/wp-content/uploads/2022/06/2022_Poster_SOCATv2022_release.pdf

Bakker, D., Alin, S. R., Bates, N., Becker, M., Feely, R. A., Gkritzalis, T., . . . others (2023). Surface ocean co2 atlas database version 2023 (socatv2023) [Dataset]. https://doi.org/10.25921/r7xa-bt92

Buongiorno Nardelli, B., R. Droghei, and R. Santoleri (2016). Multi-dimensional interpolation of SMOS sea surface salinity with surface temperature and in situ salinity data, Remote Sens. Environ., 180, 392– 402. https://doi.org/10.1016/j.rse.2015.12.052

Chau, T. T. T., Gehlen, M., and Chevallier, F. (2022). A seamless ensemble-based reconstruction of surface ocean pCO_2 and air–sea CO_2 fluxes over the global coastal and open oceans, Biogeosciences, 19, 1087–1109. https://doi.org/10.5194/bg-19-1087-2022

Chavez, F. P., Sevadjian, J., Wahl, C., Friederich, J., & Friederich, G. E. (2018). Measurements of pco2 and ph from an autonomous surface vehicle in a coastal upwelling system. Deep Sea Research Part II: Topical Studies in Oceanography, 151, 137–146

Chevallier, F. (2013): On the parallelization of atmospheric inversions of CO_2 surface fluxes within a variational framework, Geosci. Model Dev., 6, 783–790. https://doi.org/10.5194/gmd-6-783-2013

Chevallier, F., Fisher, M., Peylin, P., Serrar, S., Bousquet, P., Bréon, F.-M., Chédin, A., and Ciais, P. (2005) Inferring CO_2 15 sources and sinks from satellite observations: Method and application to TOVS data, J. Geophys. Res. Atmos., 110. https://doi.org/https://doi.org/10.1029/2005JD006390

Chevallier, F., Ciais, P., Conway, T. J., Aalto, T., Anderson, B. E., Bousquet, P., Brunke, E. G., Ciattaglia, L., Esaki, Y., Fröhlich, M., Gomez, A., Gomez-Pelaez, A. J., Haszpra, L., Krummel, P. B., Langenfelds, R. L., Leuenberger, M., Machida, T., Maignan, F., Matsueda, H., Morguí, J. A., Mukai, H., Nakazawa, T., Peylin, P., Ramonet, M., Rivier, L., Sawa, Y., Schmidt, M., Steele, L. P., Vay, S. A., Vermeulen, A. T., Wofsy, S., and Worthy, D. (2010). CO_2 surface fluxes at grid point scale estimated from a global 21 year reanalysis of atmospheric measurements, J. Geophys. Res. Atmos., 115. https://doi.org/10.1029/2010JD013887

Droghei, R., Buongiorno Nardelli, B., and Santoleri, R. (2018). A new global sea surface salinity and density dataset from multivariate observations (1993–2016), Frontiers in Marine Science, 5,

84

Feely, R. A., Takahashi, T., Wanninkhof, R., McPhaden, M. J., Cosca, C. E., Sutherland, S. C., and Carr, M.-E (2006). Decadal variability of the air-sea CO_2 fluxes in the equatorial Pacific Ocean, *J. Geophys. Res.*, 111, C08S90. https://doi.org/10.1029/2005JC003129

Feely, R. A., Sabine, C. L., Hernandez-Ayon, J. M., Ianson, D., & Hales, B. (2008). Evidence for upwelling of corrosive" acidified" water onto the continental shelf. science, 320 (5882), 1490–1492.

Friedlingstein, P., O'Sullivan, M., Jones, M. W., Andrew, R. M., Gregor, L., Hauck, J., Le Quéré, C., Luijkx, I. T., Olsen, A., Peters, G. P., Peters, W., Pongratz, J., Schwingshackl, C., Sitch, S., Canadell, J. G., Ciais, P., Jackson, R. B., Alin, S. R., Alkama, R., Arneth, A., Arora, V. K., Bates, N. R., Becker, M., Bellouin, N., Bittig, H. C., Bopp, L., Chevallier, F., Chini, L. P., Cronin, M., Evans, W., Falk, S., Feely, R. A., Gasser, T., Gehlen, M., Gkritzalis, T., Gloege, L., Grassi, G., Gruber, N., Gürses, O., Harris, I., Hefner, M., Houghton, R. A., Hurtt, G. C., Iida, Y., Ilyina, T., Jain, A. K., Jersild, A., Kadono, K., Kato, E., Kennedy, D., Klein Goldewijk, K., Knauer, J., Korsbakken, J. I., Landschützer, P., Lefèvre, N., Lindsay, K., Liu, J., Liu, Z., Marland, G., Mayot, N., McGrath, M. J., Metzl, N., Monacci, N. M., Munro, D. R., Nakaoka, S.-I., Niwa, Y., O'Brien, K., Ono, T., Palmer, P. I., Pan, N., Pierrot, D., Pocock, K., Poulter, B., Resplandy, L., Robertson, E., Rödenbeck, C., Rodriguez, C., Rosan, T. M., Schwinger, J., Séférian, R., Shutler, J. D., Skjelvan, I., Steinhoff, T., Sun, Q., Sutton, A. J., Sweeney, C., Takao, S., Tanhua, T., Tans, P. P., Tian, X., Tian, H., Tilbrook, B., Tsujino, H., Tubiello, F., van der Werf, G. R., Walker, A. P., Wanninkhof, R., Whitehead, C., Willstrand Wranne, A., Wright, R., Yuan, W., Yue, C., Yue, X., Zaehle, S., Zeng, J., and Zheng, B. (2022). Global Carbon Budget 2022, Earth System Science Data, 14, 4811–4900. https://doi.org/10.5194/essd-14-4811-2022

Garnesson, P., Mangin, A., Fanton d'Andon O., Demaria, J., Bretagnon, M. (2019). The CMEMS GlobColour chlorophyll-a product based on satellite observation: multi-sensor merging and flagging strategies, Ocean Sci., 15, 819-830, Volume 15, issue 3. https://doi.org/10.5194/os-15-819-2019

Good, S., Fiedler, E., Mao, C., Martin, M. J., Maycock, A., Reid, R., Roberts-Jones, J., Searle, T., Waters, J., While, J., and Worsfold, M. (2020). The Current Configuration of the OSTIA System for Operational Production of Foundation Sea Surface Temperature and Ice Concentration Analyses, Remote Sensing, 12. https://www.mdpi.com/2072-4292/12/4/720

Hersbach, H., Bell, B., Berrisford, P., Hirahara, S., Horányi, A., Muñoz-Sabater, J., Nicolas, J., Peubey, C., Radu, R., Schepers, D., Simmons, A., Soci, C., Abdalla, S., Abellan, X., Balsamo, G., Bechtold, P., Biavati, G., Bidlot, J., Bonavita, M., De Chiara, G., Dahlgren, P., Dee, D., Diamantakis, M., Dragani, R., Flemming, J., Forbes, R., Fuentes, M., Geer, A., Haimberger, L., Healy, S., Hogan, R. J., Hólm, E., Janisková, M., Keeley, S., Laloyaux, P., Lopez, P., Lupu, C., Radnoti, G., de Rosnay, P., Rozum, I., Vamborg, F., Villaume, S., and Thépaut, J.-N. (2020). The ERA5 global reanalysis, Q. J. Roy. Meteor. Soc., 146, 19992049. https://doi.org/10.1002/qj.3803

Ho, D. T., Law, C. S., Smith, M. J., Schlosser, P., Harvey, M., & Hill, P. (2006). Measurements of air-sea gas exchange at high wind speeds in the Southern Ocean: Implications for global parameterizations. Geophysical Research Letters, 33 (16). Retrieved 2019-06-25, from https://agupubs.onlinelibrary.wiley.com/doi/abs/10.1029/2006GL026817, https://doi.org/10.1029/2006GL026817.

Körtzinger, A. (1999). Determination of carbon dioxide partial pressure (pCO_2), edited by: Grasshoff, K., Kremling, K., and Ehrhardt, M., chap. 9, 149–158, John Wiley & Sons, Ltd. https://doi.org/10.1002/9783527613984.ch9.

Menemenlis, D., Campin, J., Heimbach, P., Hill, C., Lee, T., Nguyen, A., Schodlok, M., and Zhang, H. (2008). ECCO2: High Resolution Global Ocean and Sea Ice Data Synthesis, 2008, OS31C-1292

Naegler, T. (2009). Reconciliation of excess 14C-constrained global CO_2 piston velocity estimates, Tellus B, 61, 372–384

Pujol, M., Schaeffer, P., Faugère, Y., Raynal, M., Dibarboure, G., and Picot, N.: Gauging the Improvement of Recent Mean Sea Surface Models (2018). A New Approach for Identifying and Quantifying Their Errors, J. Geophys. Res. Oceans, 123, 5889–5911. https://doi.org/10.1029/2017JC013503.

Pujol, M.-I., Faugère, Y., Taburet, G., Dupuy, S., Pelloquin, C., Ablain, M., and Picot, N. (2016). DUACS DT2014: the new multi-mission altimeter data set reprocessed over 20years, Ocean Sci., 12, 1067–1090. https://doi.org/10.5194/os-12-1067-2016

Regnier, P., Resplandy, L., Najjar, R. G., & Ciais, P. (2022). The land-to-ocean loops of the global carbon cycle. Nature, 603 (7901), 401–410

Rödenbeck, C., Bakker, D. C. E., Gruber, N., Iida, Y., Jacobson, A. R., Jones, S., Landschützer, P., Metzl, N., Nakaoka, S., Olsen, A., Park, G.-H., Peylin, P., Rodgers, K. B., Sasse, T. P., Schuster, U., Shutler, J. D., Valsala, V., Wanninkhof, R., and Zeng, J. (2015). Data-based estimates of the ocean carbon sink variability – first results of the Surface Ocean pCO_2 Mapping intercomparison (SOCOM), Biogeosciences, 12, 72517278. https://doi.org/10.5194/bg-12-7251-2015

Takahashi, T., Sutherland, S. C., Wanninkhof, R., Sweeney, C., Feely, R. A., Chipman, D. W., Hales, B., Friederich, G., Chavez, F., Sabine, C., Watson, A., Bakker, D. C., Schuster, U., Metzl, N., Yoshikawa-Inoue, H., Ishii, M., Midorikawa, T., Nojiri, Y., Körtzinger, A., Steinhoff, T., Hoppema, M., Olafsson, J., Arnarson, T. S., Tilbrook, B., Johannessen, T., Olsen, A., Bellerby, R., Wong, C., Delille, B., Bates, N., and de Baar, H. J. (2009). Climatological mean and decadal change in surface ocean pCO2, and net sea–air CO2 flux over the global oceans, Deep-Sea Res. Pt. 2, 56, 554–577. https://doi.org/10.1016/j.dsr2.2008.12.009

Wang, X., Murtugudde, R., Hackert, E., Wang, J., and Beauchamp, J. (2015). Seasonal to decadal variations of sea surface pCO_2 and sea-air CO_2 flux in the equatorial oceans over 1984–2013: A basin-scale comparison of the Pacific and Atlantic Oceans, Global Biogeochem. Cy., 29, 597–609. https://doi.org/10.1002/2014GB005031

Wanninkhof, R. (2014). Relationship between wind speed and gas exchange over the ocean revisited, Limnol. Oceanogr.-Meth., 12, 351–362, https://doi.org/10.4319/lom.2014.12.351

Weiss, R. (1974): Carbon dioxide in water and seawater: the solubility of a non-ideal gas, Mar. Chem., 2, 203–215, https://doi.org/10.1016/0304-4203(74)90015-2

Zhang, Y., Xu, H., Qiao, F. *et al* (2018). Seasonal variation of the global mixed layer depth: comparison between Argo data and FIO-ESM. *Front. Earth Sci.* 12, 24–36. https://doi.org/10.1007/s11707-017-0631-6